G. Eitel et al., Int. J. of Design & Nature and Ecodynamics. Vol. 5, No. 4 (2010) 335–353

INVESTIGATION OF PULSATILE FLOW IN THE UPPER HUMAN AIRWAYS

G. EITEL, T. SOODT & W. SCHRÖDER
Institute of Aerodynamics, RWTH Aachen University, Wüllnerstrasse 5a, 52062 Aachen, Germany.

ABSTRACT

The pulsatile flow field in the human lung is numerically and experimentally investigated. The realistic lung geometry of a human subject was acquired down to the sixth generation of bifurcation and used as a tracheobronchial model. The numerical analysis is based on a Lattice–Boltzmann method which is particularly suited for flows in extremely intricate geometries such as the upper human airways. The measurements are performed via the particle-image velocimetry method in a transparent cast generated from the original dataset. Experimental and numerical results are analyzed in a comparative way and a thorough discussion of the three-dimensional flow structures emphasizes the unsteady character of the flow field. It is evidenced that the asymmetric geometry of the human lung plays a significant role for the development of the flow field in the respiratory system. Secondary vortex structures and their temporal formation are analyzed and described in detail for two respiration frequencies. It is shown that the qualitative structure of the intricate flow field does not vary if a critical mass flux rate is exceeded. At inspiration, the primary flow shows separated flow regions and is highly influenced by secondary flow structures. By contrast, at expiration the primary flow distribution is far more homogeneous with a higher level of vorticity.

Keywords: counter-rotating vortices, human airways, Lattice–Boltzmann method, particle-image velocimetry, pulsatile flow, transparent lung cast.

1 INTRODUCTION

The human lung is a highly complex respiratory system consisting of a repeatedly bifurcating pipe network at progressively decreasing diameters. It fulfills multiple tasks in conjunction with the nasal cavity, *viz.*, the air transport and the exchange of carbon dioxide and oxygen in the pulmonary alveoli. Furthermore, at inspiration the air has to be heated up and moisturized and solid particles are removed from the flow. At expiration the loss of heat and humidity has to be limited. Thus, the requirements are challenging and several processes take place at the same time inside the respiratory tract.

The understanding of flow processes in the upper human airways is of great importance to develop aerosol drug delivery systems and to improve the efficiency and usability of artificial respiration systems. Numerous experimental and numerical investigations of lung flow have been conducted so far [1–4]. However, due to the high geometric intricacy of the human lung, there is still a considerable amount of uncertainty concerning the very complex flow field and fundamental results for realistic lung models are still rare. Many investigations are based on simplified models of the lung structure. The most popular of these models is the so-called Weibel model [5] which describes the bronchi as a symmetric tree structure of subsequent bifurcating pipes consisting of 23 generations. However, in most of the studies only the first three to five generations are considered and a planar representation is favored for simplicity. In Ref. [1] detailed experimental studies were performed for a planar Weibel model where fundamental flow phenomena like m-shaped velocity profiles and counter-rotating vortices were described. It was shown in numerical studies [2, 6], however, the flow field for the non-planar configuration differs significantly from the planar case. Studies considering asymmetric bifurcations [3], non-smooth surfaces [7] and CT-based models [4, 8, 9] show that the inspiration flow in the upper human airways is asymmetric and swirling. These results emphasize the importance of realistic airway models.

ISSN: 1755-7437 (paper format), ISSN: 1755-7445 (online), http://journals.witpress.com
DOI: 10.2495/DNE-V5-N4-335-353

Generally, the aforementioned results show that an accurate lung geometry, i.e. CT data or a real human lung cast, is required to obtain physiologically relevant results. Grosse *et al.* [10, 11] experimentally investigated the steady and oscillating flow field in a silicon model of a human lung cast that covers the trachea and the bronchial tree down to the sixth generation. It was found that the flow structures mainly depend on the instantaneous Reynolds number and on the Womersley number. In the experiment only a parallel cutting plane could be taken into account, so the investigation of vortical structures was limited to a detailed qualitative analysis.

The present work focuses on the investigation of the unsteady three-dimensional flow for the lung model used by Grosse *et al.* [10] for a normal respiration at rest and for an increased rate of respiration. Numerical results are compared with experimental findings and flow structures are described in detail. The flow field is simulated via a Lattice–Boltzmann method (LBM) [12]. Unlike former numerical investigations, in which a simplified geometry was used, the present method can be efficiently applied to variable, realistic airway geometries. For instance the flow field downstream of the laryngeal region was recently investigated in Refs. [13, 14] by LBM. In combination with an automated grid generation [15] based on CT-data this method offers an efficient tool for biomedical flow problems. Since the numerical method is capable of reproducing small-scale features of the entire lung flow, the results support to fundamentally understand respiratory mechanisms. Thus, the numerical results allow an extended analysis of the three-dimensional flow structures observed in the experiment.

However, despite a long-term experience in the development and application of computational fluid dynamics methods to mechanical engineering problems, it is still a must to ensure the quality of the numerical solutions. In the present work, particle-image velocimetry measurements are used for the validation. The results mainly serve to fundamentally understand the three-dimensional flow structures and the time-dependent development within the upper bifurcations of the human lung under normal breathing conditions.

The structure of this paper is as follows. First, a concise description of the fundamental fluid mechanics is given. Then, the lung model, the experimental setup, and the numerical method are specified. Subsequently, numerical and experimental results are compared and discussed. Finally, the findings are summarized and some conclusions are drawn.

2 FUNDAMENTAL FLUID MECHANICS

In the following, the flow is assumed laminar and incompressible.

2.1 Steady flow in curved pipes

Since flows through bended pipes possess curved path-lines, centrifugal forces and pressure gradients normal to the axis of the pipe exist. This pressure gradient reads

$$\frac{\partial \rho}{\partial n} = -\rho \cdot \frac{u^2}{r_c} \, . \tag{1}$$

The expressions $\partial \rho / \partial n$, ρ, u, and r_c represent the pressure gradient normal to the streamwise direction, density, streamwise velocity component, and curvature radius, respectively. Higher axial velocities on the axis of the pipe cause higher centrifugal forces, i.e. the core flow is directed to the outer wall (O). The near-boundary fluid is displaced and moves near the pipe wall towards the inner part (I) (see Fig. 1). A secondary flow structure with velocities perpendicular to the pipe axis develops. The shift of the velocity maximum towards the outer wall enhances the pressure gradient

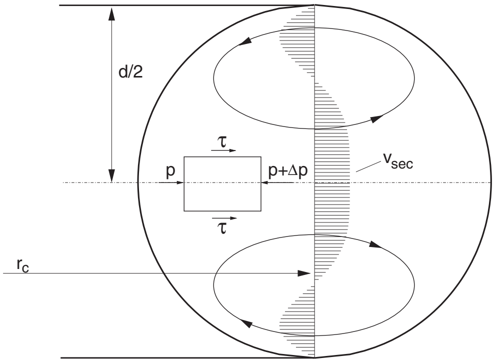

Figure 1: Illustration of the secondary velocity v_{sec} in a bended pipe with diameter d and curvature radius r_c. The shear stress τ, and the pressure ρ are denoted for an evanescent volume on the plane of symmetry.

increasing the probability of flow separation [16]. For the steady flow case Dean [17, 18] has analytically described the development of two counter-rotating vortices. He proved that the flow can be characterized by the Dean number $De = Re \cdot (d/r_c)^{1/2}$ where d represents the pipe diameter and Re is the Reynolds number $Re = d\bar{u}/\nu$ based on the mean streamwise velocity and the kinematic viscosity ν. Various publications (e.g. [19, 20]) intensively investigated this phenomenon and substantiated the fundamental understanding of bended pipe flows.

2.2 Pulsatile flows

In pulsatile flows the relationship between the applied pressure and the flow rate depends on the frequency. An exact theory for a time dependent flow in a long straight rigid and circular pipe under a periodic pressure gradient has been introduced by Womersley [21]. Regarding the oscillation frequency f a dimensionless number $\alpha = 0.5d\sqrt{2\pi f/\nu}$, called Womersley number, can be derived. This number describes the development of velocity profiles in a viscous fluid with an alternating pressure gradient for different frequencies. For $\alpha > 1$ inertia effects arise which affect the velocity profile. First, the core flow becomes broader at increasing Womersley number, i.e. the velocity profile is flattened. Second, the near-wall flow is transiently reversed. This is illustrated by analytical results for different phase angles $-\pi/2 < \phi < 0$ in Fig. 2a for $\alpha = 3.64$ and in Fig. 2b for $\alpha = 5.15$. The distributions are calculated for a pipe with a hydraulic diameter of $d_{\text{hyd}} = 4A/U = 18.3$ mm where A is the cross section area and U is the circumference of the pipe. The fluid properties are based on a water–glycerin mixture as used in the experiment. The temporal change of the pressure drop along the axis of the pipe is assumed to be sinusoidal. Due to inertia effects the mean flow lags the pressure gradient by about 90° at $\alpha > 10$. Note that in bifurcating pipe systems at decreasing radius the local Womersley number decreases monotonically.

3 THE LUNG MODEL

The geometry for the numerical investigations is based on a radiological scan taken from a cast of a human lung including the larger part of the trachea down to the sixth generation of the bronchial tree. The digital geometry reconstruction encompasses the pre-processing, the segmentation, the surface generation, and the iterative surface smoothing. Based on the surface data a computational mesh is automatically generated by an in-house grid generator.

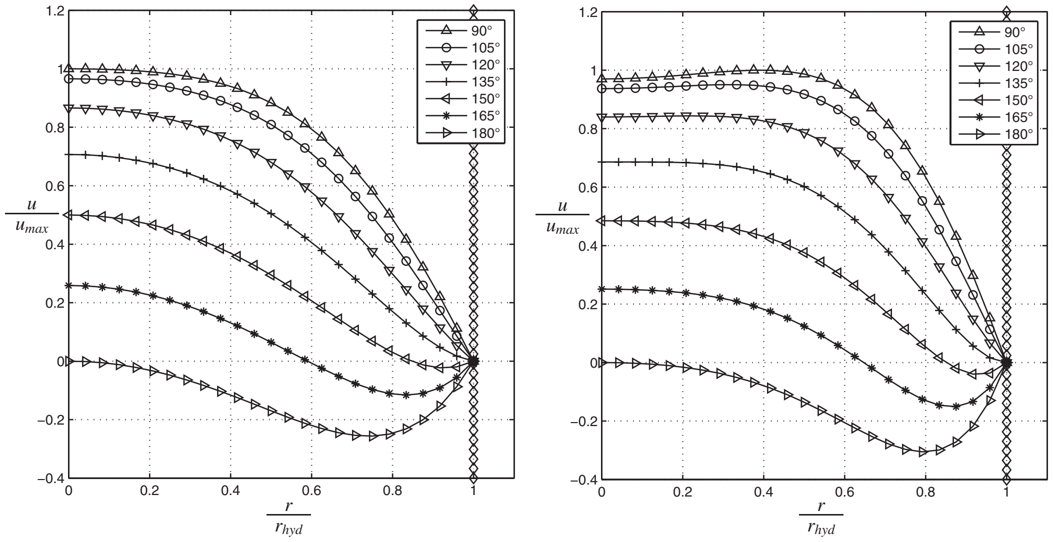

(a) (b)

Figure 2: Temporal development of velocity profiles of circular pipe flow under a sinusoidal pressure gradient for (a) $\alpha = 3.64$ and (b) $\alpha = 5.15$. The normalized velocity $u/u_{\max}$ is plotted vs. the normalized radius r/r_{hyd}, where $u_{\max}$ is the maximum streamwise velocity and r_{hyd} is the hydraulic radius. The symbols $\triangle$, $\circ$, ∇, $+$,$\lhd$, $*$, $\rhd$ denote the phase angles from 90° to 180° and $\diamond$ denotes the wall.

The same lung data was used to generate the silicon model for the PIV measurements in several manufacturing processes including corn starch rapid prototyping, surface coating, inlet insert attachment, transparent silicon (RTV815) casting, hot water wash-out, and manual channel drilling of the model's exits. These steps lead to models which allow flow field measurements within organic geometries and give the opportunity to understand *in vivo* flow phenomena.

The geometry is simplified in the sense that any elasticity of the configuration is not considered. However, the upper airways, as they are modeled here, are supported by chondral springs and can be assumed as the stiffest part of the lung. The physiological lung is an enclosed system with spatially varying tissue properties that lead to non-linear pressure–volume relations. The resulting spatial pressure distribution yields equilibrium processes which cannot be accounted in a model having open ends. At the tracheal cross section a fully developed laminar inflow is imposed by a Dirichlet boundary condition in the numerical analysis and by an extended trachea in the experiment.

Assuming a static geometry and neglecting any compliance influence of the lower lung parts, the present method delivers a fundamental insight into the lung flow, including the propagation of ventilation, frequency dependent spatial and temporal mass flow rates, shear stresses, dead water regions, and secondary flow structures. Fig. 3a shows the final experimental model from a dorsal point of view and in Fig. 3b the model of the numerical simulation is illustrated.

4 EXPERIMENTAL SETUP

In the following the specifications of the experimental setup and the measuring parameters are discussed. The current study extends the investigation by Grosse *et al.* [10]. That is, in greater detail the

(a) (b)

Figure 3: The employed lung model: (a) silicon model for PIV measurements and (b) surface data and computational grid.

three-dimensional flow structure and the pulsatile flow field are addressed. The ventilation is sinusoidal and represents human breathing at rest. The particle-image velocimetry (PIV) measurements of the human lung flow were performed in a 1:1 realistic lung cast based on computer tomography data.

The test rig schematically shown in Fig. 4a is designed as an open system containing a linearly actuated piston, a transparent container, an inflow pipe and equalizing tank. The pulsatile volume flux is generated by an assembly consisting of a motor prototype (MOOG Inc., Böblingen, Germany)

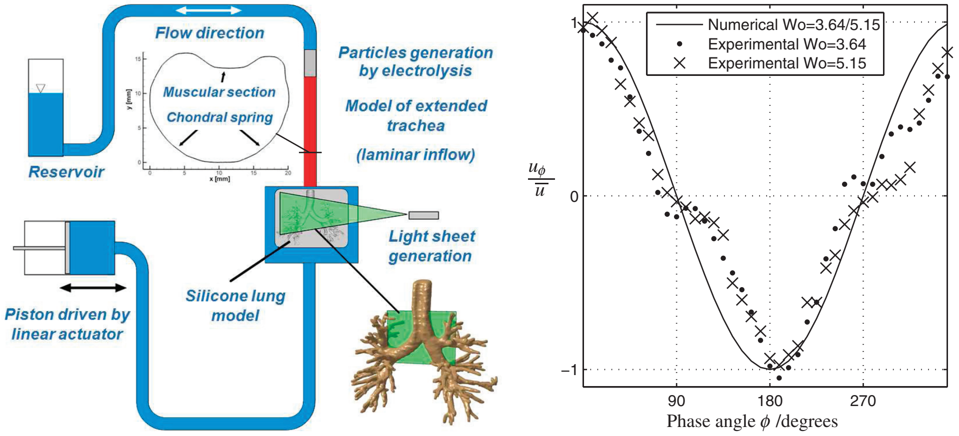

(a) (b)

Figure 4: (a) Schematic of the experimental setup; (b) Normalized bulk velocities of the inflow for phase angles between $0° < \phi < 351°$ and Womersley numbers of $\alpha_1 = 3.64$ (·) and $\alpha_2 = 5.15$ (×). The solid line denotes the ideal sinusoidal curvature used in the numerical analysis.

and a self-made piston. The amplitude A and the frequency f are adjusted in a range of A = 0–1.51/s and f = 0–3 Hz, respectively. The model is centered in the container at high distances to the PMMA (Plexiglas®) walls such that optical accessibility for the laser generated light sheet and the perpendicular mounted CCD camera (Sensicam QE, PCO, Kehlheim, Germany) is guaranteed and heterogeneous inflow conditions for the expiration phase can be neglected. The inflow pipe has a length of L = 500 mm, an anatomical inner contour matching the upper part of the shape of the trachea and a hydraulic diameter of approximately d_{hyd} = 18.3 mm. The length to diameter ratio of $L/d_{\mathrm{hyd}} = 27$ ensures a fully developed laminar velocity profile. The junction between the inlet pipe and the entry of the model can be assumed smooth such that no incipient flow separation occurs. The system is totally filled up by a fluid solution of water and glycerin. The glycerin fraction of the mixture is 60.7 mass percent to match the refraction index (n = 1.44) of the model's silicon. This kind of adaption leads to an optical access without distortion.

At a measurement temperature of T = 25°C the dynamic viscosity is $\eta = 9.1 \times 10^{-3}$ Pa·s, the density is $\rho = 1.153 \times 10^{3}$ kg/m^3, and the kinematic viscosity is $\nu = 7.89 \times 10^{-6}$ m^2/s.

Due to the properties of the linear actuator the Reynolds number of $Re_{\max}$ = 1,600 can be achieved at both Womersley numbers $\alpha_1 = 3.64$ and $\alpha_2 = 5.15$. An electrolysis unit located between the model's inlet and the reservoir generates hydrogen bubbles in the size of d_b = 1–5 µm which are used as tracer particles. By changing the electrolysis voltage, the amount of saline addition, and the seeding time of the total amount of bubbles can be adjusted. The bubble lifetime ranges from 10 to 30 min which is large compared to the measuring time. The illumination of the tracers is done by an approximately 1 mm thick light sheet which is generated by a Nd:YAG-Laser (Minilite, Continuum, Inc., Darmstadt, Germany) with a nominal power of 25 mJ. The laser beam is widened by optical devices to cover the region of interest which is fully captured by a double shutter CCD camera (resolution: 1,376 × 1,040 px). The calibration of the light sheet position was conducted by photometric comparison of the recorded images at different parallel positions with shifted slices of the numerical data set and by using a calibration target. The target also provides a gauge for the camera captured pixel distance. Normalized bulk velocities, measured at a distinct inflow section, are plotted in Fig. 4b for all recorded phase angles and both Womersley numbers. The deviations result from the non-optimal tracking between the motor's lift change and the fluid flux. Therefore, the arrangement of experimental and numerical data is based on the Reynolds similarity.

Images were captured every 9 degrees of one ventilation cycle with 200 records at each phase angle. This procedure was pursued for both Womersley numbers in three different measurement planes. Analyses including cross-correlating, filtering, adaptive cross-correlation, interpolation, and averaging were processed by the commercial software VidPIV (ILA GmbH, Jülich, Germany). The results contain velocity and vorticity distributions with a spatial resolution of R = 2.32 vectors/mm in both dimensions.

5 THE LATTICE–BOLTZMANN METHOD

Next, the Lattice–Boltzmann Method (LBM) is concisely described. The LBM is a solution algorithm for non-linear partial differential equations and it arose from Lattice Gas Cellular Automata (LGCA) which was introduced by Frisch *et al.* [22] in 1986. It was shown by the authors that a microscopic model describing molecular dynamics with collisions which conserve mass and momentum leads in the macroscopic limit to the Navier–Stokes equations if the underlying lattice possesses a sufficient symmetry. An extensive description of both methods, the LGCA and the LBM, is given in Refs. [12, 23, 24]. The most common variant of the LBM is based on the Boltzmann equation with a simplified collision operator proposed by Bhatnagar *et al.* [25] called BGK equation. The velocity space is discretized into a set of n molecular velocities c_i with their associated distribution functions $f_i(x,t)$. The discrete BGK equation without external forcing reads

$$f_i(x + c_i \Delta t, t + \Delta t) - f_i(x,t) = \omega(f_i^{eq} - f_i), \tag{2}$$

where f^{eq} is the Maxwell equilibrium distribution function and ω represents the collision frequency. The corresponding numerical method is referred to as LBM–BGK method. The left-hand side of eqn (2) contains the temporal change and the propagation term, whereas the right-hand side describes molecular collisions by a relaxation of the distribution functions towards thermodynamic equilibrium. Therefore, the algorithm of the flow solver is based on the iterative computation of propagation and collision processes for all cells of the computational grid. The macroscopic values of density ρ and momentum j are obtained as base moments of the distribution function which read

$$\rho(x,t) = \sum_{i=1}^{n} F_i(x,t) \tag{3}$$

$$j(x,t) = \rho(x,t)v(x,t) = \sum_{i=1}^{n} c_i F_i(x,t). \tag{4}$$

The LBM–BGK describes weakly compressible flows at moderate Reynolds numbers and it has been shown in the literature [26] that it yields indeed solutions to the Navier–Stokes equations. LBM models are characterized by the number of spatial dimensions m and the number of discrete velocities n. Therefore, the DmQn notation was introduced by Qian *et al.* [27]. Favored models in two and three dimensions are D2Q9, D3Q19, and D3Q27, since they offer sufficient lattice symmetry. The discrete velocity set for the D3Q19 model is shown in Fig. 5.

Since the LBM formulation is based on a uniform Cartesian mesh, it is highly adapted for parallel processing and it offers an efficient boundary treatment for fixed walls. The ability of reproducing variable organic geometries makes this method well suited for biomedical applications.

In this study the flow in the upper human airways was simulated by a D3Q19 LBM–BGK model with a modified equilibrium distribution function for incompressible flows as proposed by Zou *et al.* [28]. Solid wall nonslip boundary conditions were realized by an interpolated bounce-back rule [29]. A Dirichlet boundary condition imposing a fully developed laminar velocity profile was prescribed at the tracheal cross section, whereas a zero gradient condition was employed at the numerous

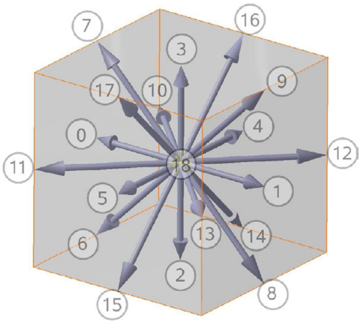

Figure 5: The discrete velocity set of the D3Q19 model.

outlets. The computational grid was automatically generated from surface data by an in-house grid generator [15] and consists of 2.5 million cells. It was shown, e.g. in Ref. [14] that the numerical method allows a detailed investigation of the three-dimensional flow field in the primary bronchi.

6 RESULTS

The time dependent inhalation and exhalation flow field has been investigated for a peak mass flux of 351 ml/s corresponding to a peak Reynolds number of $Re_{\max} = 1{,}600$. The value of the Reynolds number is based on the hydraulic diameter of the trachea $d_{\mathrm{hyd}} = 18.3$ mm. To investigate the unsteady behavior of the flow field during respiratory ventilation, simulations and measurements were performed for a normal respiration at rest at frequency f_1 and for a higher respiration frequency $f_2 = 2f_1$. That is, the breathing periods are $T_1 = 4$ s and $T_1 = 2$ s which correspond to Womersley numbers $\alpha_1 = 3.64$ and $\alpha_1 = 5.15$, respectively.

The temporal variation of the mass flux was prescribed by a sinusoidal curve as shown in Fig. 4b. The data were recorded after a transient time of one respiration cycle. In the following section numerical and experimental results are compared in a distinct cross section. Subsequently, the numerical data is further analyzed concerning the development of the three-dimensional flow structures.

6.1 Comparison of experimental and numerical data

In this section numerical and experimental data are compared in order to evidence the quality of the LBM solution. A brief comparison is presented for one plane of the first bifurcation which is defined in Fig. 6a. This region was chosen to globally evidence the mass flux into the lower bifurcations. Moreover, the phase angles at maximum inspiration and expiration can be compared with steady flow cases.

The comparison of the data at α_1 and α_2 shows no significant differences in the flow structures in this plane, which is why in the following only the solutions at $\alpha_1 = 3.64$ are discussed. Figures 7 and 8 contain numerical and experimental results at different phase angels ϕ of a sinusoidal ventilation cycle, where $\phi = 0°$ and $\phi = 180°$ represent maximum inspiration and expiration, respectively.

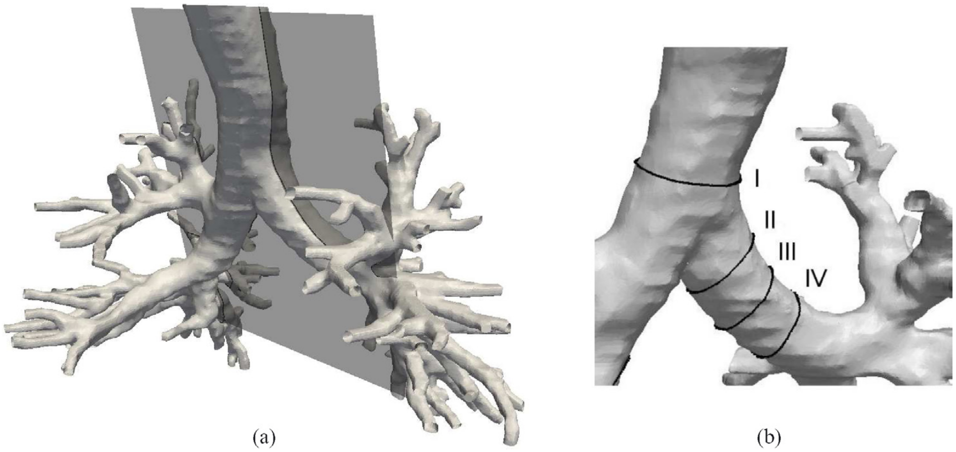

(a) (b)

Figure 6: (a) Reference plane for the comparison of experimental and numerical data. (b) Cross sections for the investigation of secondary flow structures.

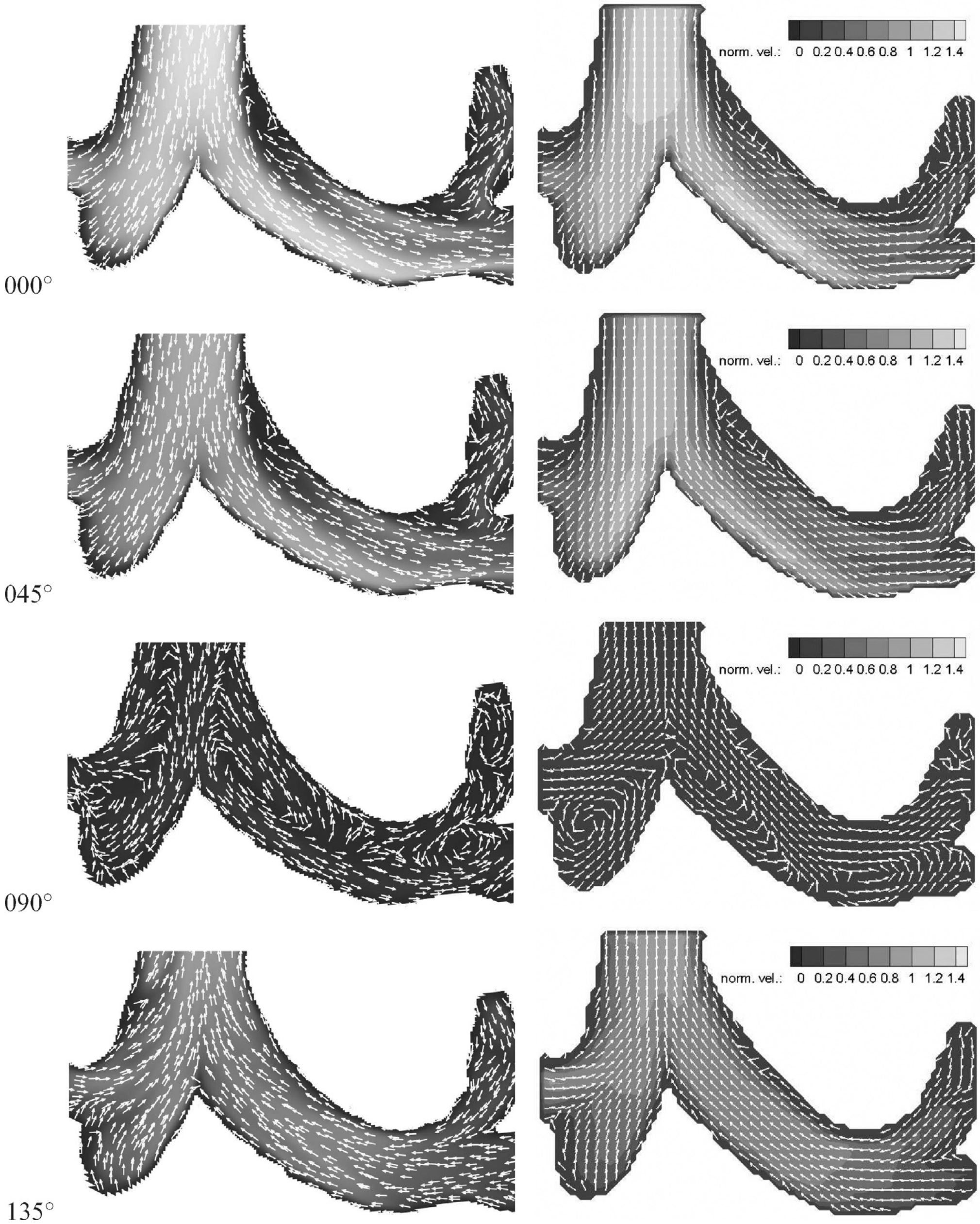

Figure 7: Time resolved data for the first half of a respiration cycle at rest, i.e. $\phi = 0°, 45°, 90°, 135°$; LBM data (left), PIV data (right). The vectors have uniform length and indicate the flow direction. The gray scale values show the magnitude of the absolute velocity that is normalized by the bulk velocity at maximum inspiration for a defined tracheal section.

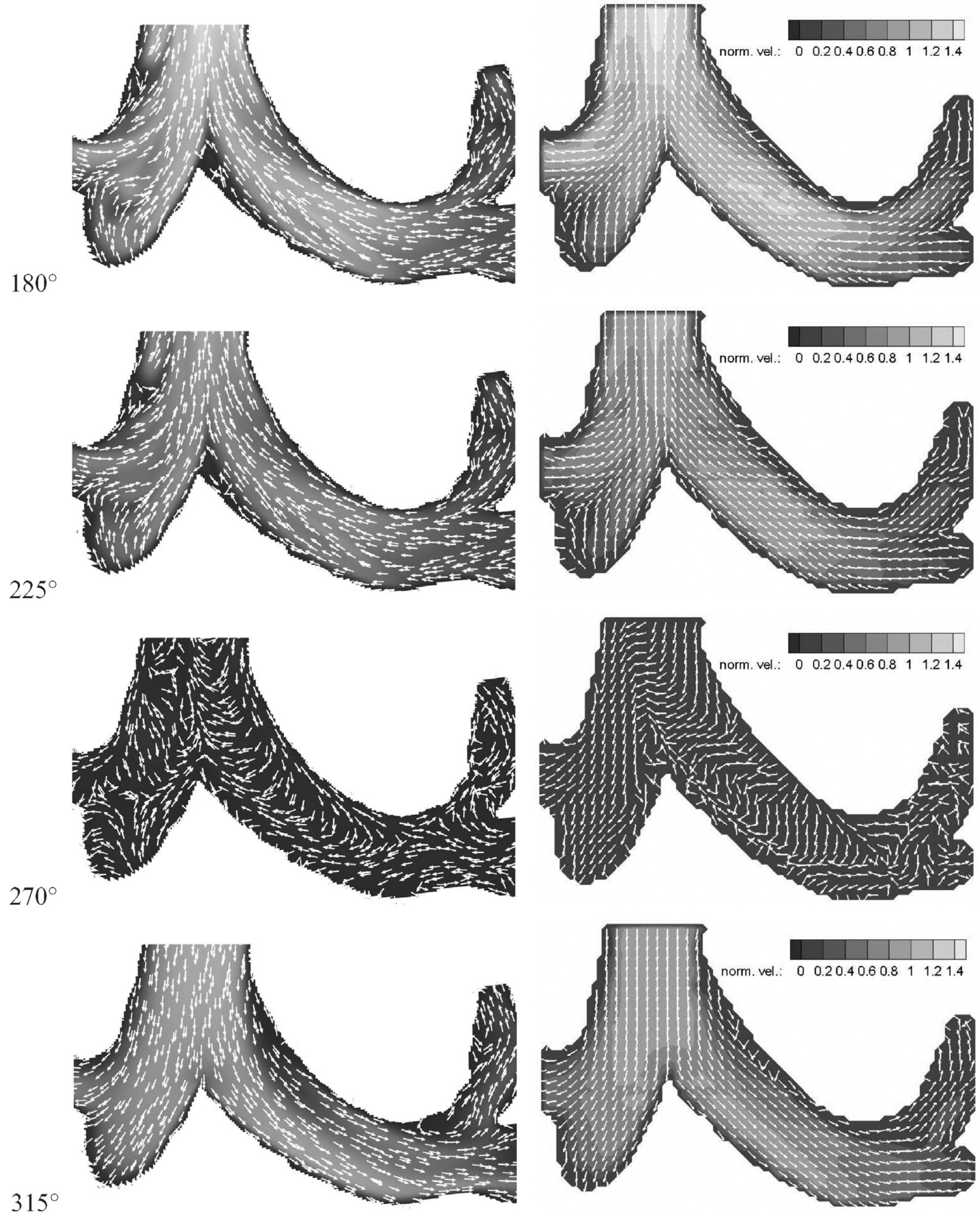

Figure 8: Time resolved data for the second half of a respiration cycle at rest, i.e. $\phi = 180°, 225°, 270°, 315°$; LBM data (left), PIV data (right). The vectors have uniform length and indicate the flow direction. The gray scale values show the magnitude of the absolute velocity that is normalized by the bulk velocity at maximum inspiration for a defined tracheal section.

To emphasize the flow direction the vectors possess uniform length. The magnitude of the absolute velocity is normalized on the bulk velocity in cross section I in Fig. 6b at maximum inspiration. In the following, the terms *upper* and *lower* denote the upper and lower half of the main bronchi (bronchi principales), respectively. Note that there is a third sub-branch at the end of the posterior right main bronchus. The subsequent discussion of the numerical and experimental findings for various phase angles $\phi = 0°, 45°, 90°, 135°, 180°, 225°, 270°, 315°$ shows the quality of the solutions of the Lattice–Boltzmann method under pulsatile flow conditions.

$\phi = 0°$: The flow field is almost identical with the steady case distribution which was extensively discussed in Ref. [14]. A distinct stagnation point occurs at the first bifurcation (carina tracheae). The LBM and PIV solutions possess a high-speed region near the lower wall which is very similar in extension and magnitude. A closer look indicates that the high-speed region reaches somewhat further into the next branch. Curvature induced separations at the upper wall near the main bronchial entry also do occur in the simulation and in the measurement. The structures of the sub-bronchial flow field are similar in both cases.

$\phi = 45°$: Compared to $\phi = 0°$ the velocity magnitude is globally reduced whereas the flow structures remain almost alike. The numerical solution possesses slightly higher peak values of velocity.

$\phi = 0°$: At this phase angle the inspiration ends and the expiration phase sets in. The high-speed region near the lower wall still exists, whereas the outflow is already established in the upper part of the bronchus. The resulting mixing layer is evident in the numerical and experimental findings. The illustrations show similar recirculation regions for the LBM and PIV data.

Nevertheless, there are some differences which occur especially in the tracheal flow pattern and in the extension of the high-speed region. This discrepancy is due to a phase shift, i.e. the simulation slightly lags the experiment. It is clear that during transition from inspiration to expiration the impact of a little difference in the numerical and experimental description is more pronounced. This is visualized in Fig. 7 at $\phi = 90°$.

$\phi = 135°$: At this stage all inflow patterns have disappeared. A nearly homogeneous outflow from all sub-branches is observed such that is indicating an almost perfect wash-out.

$\phi = 180°$: At higher phase angles the outflow develops a more pronounced velocity distribution, i.e. the peak velocity and the bulk velocity differ clearly. This flow pattern is caused by the sub-branches since five high-speed streaks merge in the trachea. Only in the numerical solution a small recirculation region on the lower wall of the left bronchus is observed which interacts with the mainstream in the trachea. This discrepancy is likely to be due to slight deviations of the curvature of the lower wall in the final silicone model and the original lung data.

$\phi = 225°$: From $\phi = 180°$ to $\phi = 225°$ the overall flow structures do not change. Only the velocity magnitude is reduced.

$\phi = 270°$: The flow pattern characterizes the change from expiration to inspiration. It is clear that the simulation possesses a slight delay to the experiment. The simulation results evidence that inspiration first sets in near the upper walls of the primary bronchi.

$\phi = 315°$: The inspiration flow pattern is similar to the structure at $\phi = 0°$ although the separation regions are spatially reduced and the high-speed region is broader than at full inspiration ($\phi = 0°$).

In conclusion, the numerical and experimental data match satisfactorily. The slight differences of the LBM and PIV data are due to small deviations of the lung model and the original geometry data. Moreover, the discrepancies near the wall appear to be caused by a lack of seeding particles in the flow regimes resulting in a decreased resolution of the velocity distribution. Finally, the boundary conditions of the numerical and the experimental setup do not perfectly coincide, since the pipe extensions downstream of the sixth generation are not taken into account in the simulation and the temporal change of the volume flux is not perfectly sinusoidal in the experiment. Keeping these facts in mind, the numerical–experimental agreement can be considered convincing.

6.2 Secondary flow structures

In order to obtain a deeper insight into the development of the flow pattern, the secondary flow structures are further analyzed in this section on the basis of the numerical solutions. The locations of the various cross sections denoted by I, II, III, and IV are defined in Fig. 6b. The flow field in the trachea is depicted for both Womersley numbers in Fig. 9 at maximum inspiration ($\phi = 0°$) and in Fig. 10 at maximum expiration ($\phi = 180°$). The black lines indicate the reference plane of the flow patterns which were discussed in the previous section.

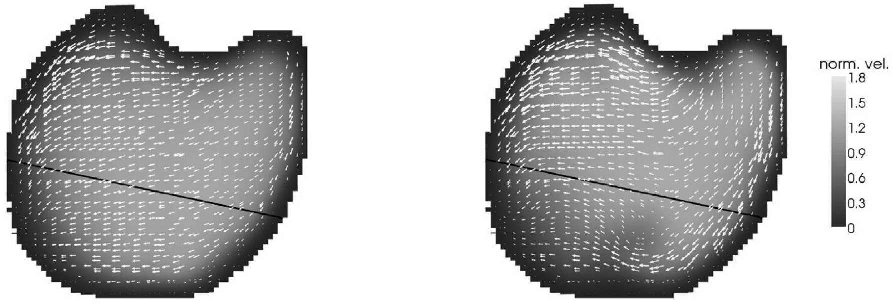

(a) (b)

Figure 9: Flow field in the tracheal cross section I described in Fig. 6b at maximum inspiration; (a) $\alpha_1 = 3.64$ and (b) $\alpha_2 = 5.15$. The levels of gray indicate the axial velocity magnitude and the arrows represent the in-plane velocity. The black lines indicate the reference plane described in the previous section.

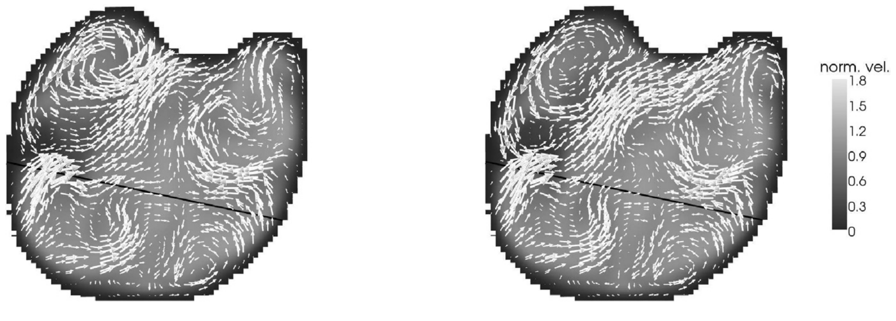

(a) (b)

Figure 10: Flow field in the tracheal cross section I described in Fig. 6b at maximum expiration; (a) $\alpha_1 = 3.64$ and (b) $\alpha_2 = 5.15$. The levels of gray indicate the axial velocity magnitude and the arrows represent the in-plane velocity. The black lines indicate the reference plane described in the previous section.

At maximum inspiration a well developed velocity profile is observed at α_1 the shape of which is characterized by the geometry of the throat. At α_2 the velocity distribution possesses clear deformations compared to the α_1 profile. At maximum expiration strong vortical structures occur over the whole cross sections which are shown in Fig. 10. These structures are generated by the asymmetric merging of the air streams from the left and right principal bronchus. A stagnation point is observed near the right wall just above the reference plane. Note that unlike the inspiration structures the expiration structures show no significant dependence on the Womersley number.

In Fig. 11 the flow field at maximum inspiration and expiration at $\alpha_1 = 3.64$ is depicted in the cross sections II–IV. At inspiration the main mass flux is located near the lower wall. This corresponds to

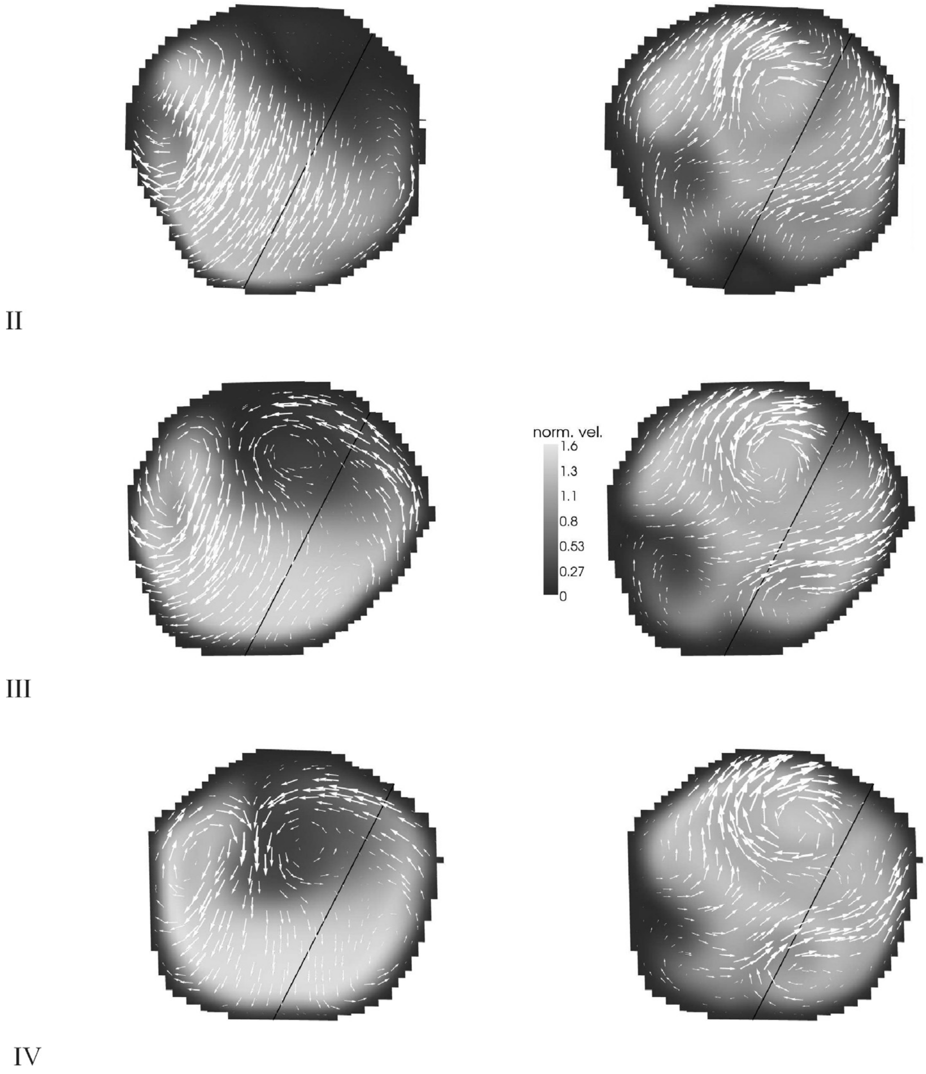

Figure 11: Flow field in the cross sections II–IV; inspiration (left), expiration (right). The axial velocity is shown by gray scale values and the arrows represent the in-plane velocity. The black lines indicate the reference plane described in the previous section.

the high velocity region shown in Fig. 7 at $\phi = 0°$. Downstream of the first bifurcation a pair of counter-rotating vortices develops transporting fluid from the high-speed to the low-speed region along the outer walls. The right vortex has a center of rotation near the upper wall and covers most of the upper half of cross section IV. The left vortex is much smaller and it is located very close to the left wall. Such a vortex pair also was observed in the steady state simulations in Ref. [14]. The physics of its generation is related to the aforementioned Dean vortex. Once the next bifurcation is reached, the vortices do separate and each one enters a branch of the next higher bronchial generation.

At expiration the streamwise velocity is more evenly distributed than at inspiration. The mixing of streams coming from the higher generation bronchi generates a shear layer which yields a swirling region. Two stagnation regions are indicated in Fig.11. One is located at the lower wall and develops in the streamwise direction. The other stagnation region occurs at the left wall and vanishes when the trachea is approached. The in-plane velocity distribution evidences a strong clockwise rotating vortex near to the upper wall and more mass flux is coming from the ventral lung lobe.

In conclusion, the findings confirm pronounced secondary flow structures at inspiration and expiration. The numerical data emphasizes the strong asymmetry of the vortical structures. It is clear that the vortical flow structures are more intricate at expiration ensuring an almost perfect wash-out.

To show the temporal variation of the vortical structures the axial vorticity component in cross section IV was determined over a whole respiration cycle. The mean magnitude of the axial vorticity versus the phase angle ϕ is shown in Fig. 12 for both Womersley numbers. The amount of vorticity clearly increased at higher Womersley number at inspiration. A slight phase shift is also evident

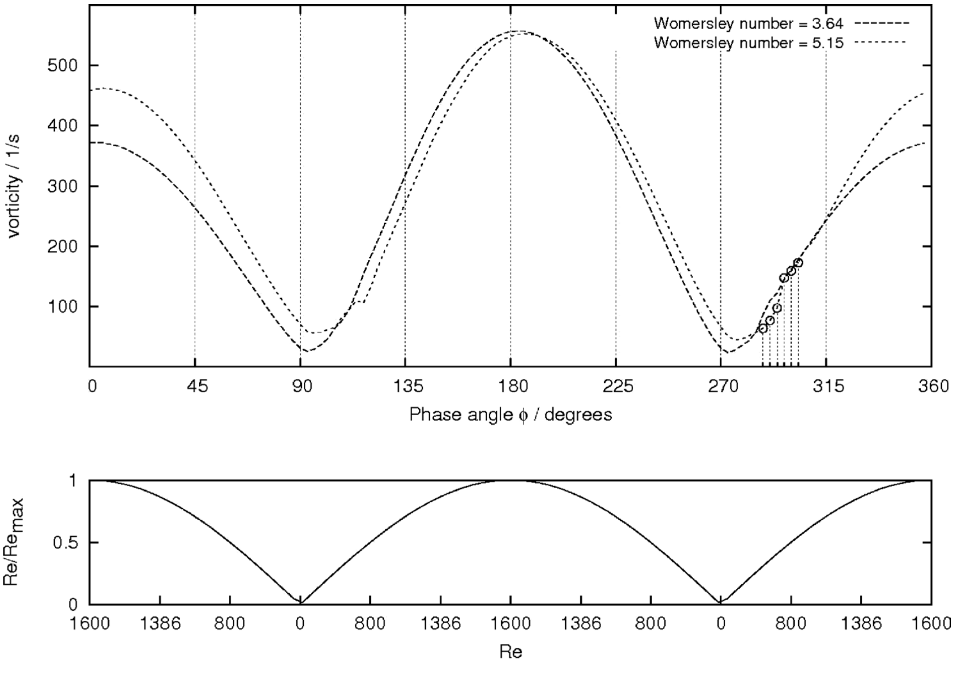

Figure 12: (Top) Mean in-plane vorticity magnitude plotted against the phase angle for the cross section IV in Fig. 6b. (Bottom) $Re/Re_{\max}$ as a function of the Reynolds number which varies with ϕ.

between the two curves indicating that vortical structures appear at higher Reynolds number, if the Womersley number is increased. This is in agreement with pulsatile flow theory and was also observed by Grosse *et al.* [10] who found the critical Reynolds number Re_C for the creation of vortical structures to increase when the frequency of respiration is set to higher values. The level of vorticity in this distinct plane is higher at expiration than at inspiration which is in agreement with the observed intricate flow structures. At α_2 the slope of the vorticity increases at a certain point during incremental inspiration which is highlighted in Fig. 12.

The temporal evolution of the flow field is analyzed in cross section IV at α_2. Figures 13 and 14 show the solutions for six phase angles at the very beginning of inhalation. The corresponding points

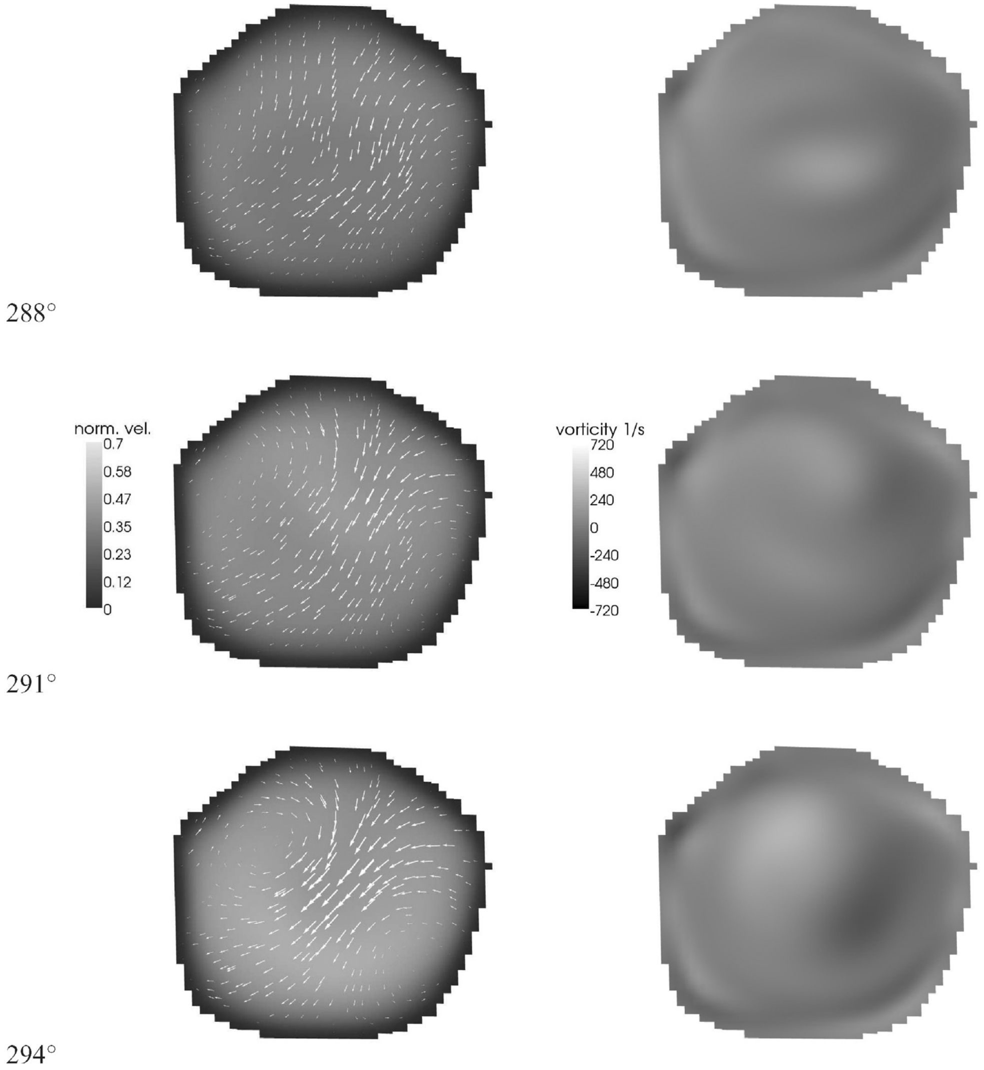

Figure 13: Distributions of velocity (left) and vorticity (right) in cross section IV in Fig. 6b at early inspiration for $\alpha_2 = 5.15$. The arrows describe the in-plane velocity field and the levels of gray represent the magnitude of the axial velocity and the axial vorticity, respectively.

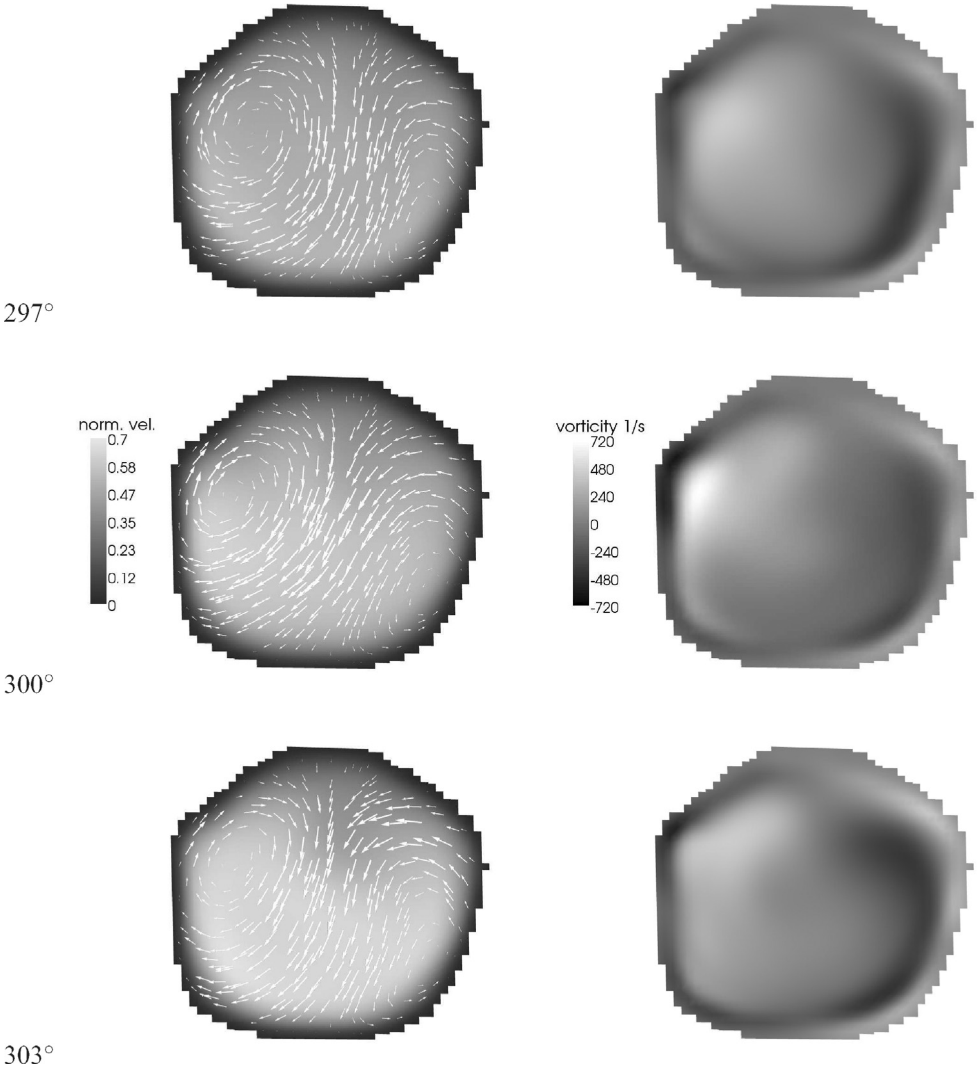

Figure 14: Distributions of velocity (left) and vorticity (right) in cross section IV in Fig. 6b at early inspiration for $\alpha_2 = 5.15$. The arrows describe the in-plane velocity field and the gray scale values represent the magnitude of the axial velocity and the axial vorticity, respectively.

are highlighted in Fig. 12. The sequence starts 12.5 ms after the bulk velocity at the inlet cross section has reversed and covers 10.4 ms. At $\phi = 288°$ the distribution of the axial velocity shows a rather flat pattern and the vortical structures are still defined by those at maximum expiration, i.e. the clockwise rotating vortex is still there. At $\phi = 297°$ counter-rotating vortical structures form throughout the cross section and an incipient asymmetry of the axial velocity distribution is indicated, i.e. the location of the peak value occurs close to the lower wall. In the following time intervals the vorticity increases rapidly. Finally, the counter-rotating vortices and the axial velocity distribution at $\phi = 303°$ are already very similar to those observed at maximum inspiration. The increase of vorticity at early inspiration is thus caused by the formation of the counter-rotating vortex pair. The same process also is detectable for α_1.

The numerical results show that the fundamental vortical structures and the high-speed region which have been observed at maximum inspiration are already encountered at $Re_C\,(\alpha_1) = 414$ and $Re_C\,(\alpha_2) = 651$. This is in agreement with the experiment where the size of the counter-rotating vortices has been found to be independent of the Reynolds number as long as the Reynolds number is above a critical level.

7 SUMMARY AND CONCLUSIONS

The pulsatile flow field in a geometrically realistic model of the human lung was numerically and experimentally investigated for two Womersley numbers, $\alpha_1 = 3.64$ and $\alpha_2 = 5.15$, and a maximum Reynolds number of $Re_{\max} = 1{,}600$. The Lattice–Boltzmann method proved to be an accurate tool to simulate flows through highly intricate geometries such as the upper human airways. The numerical findings were validated by particle-image velocimetry measurements. The overall flow structure at inspiration, which is characterized by local recirculation regions, and at expiration, which evidences a more homogeneous velocity distribution, was shown to be in convincing agreement. Secondary flow structures known from steady state simulations were clearly identified. A pair of counter-rotating vortices and a high-speed region were observed downstream of the first bifurcation in the left bronchus.

The growth of the vortical structures in the left branch of the first bifurcation was investigated in detail with respect to incipient inspiration. After reversal of the flow, the formation of secondary flow structures remains until the Reynolds number reaches a critical value. Above this value the overall flow structure remains qualitatively the same. The critical mass flux rate for the development of the characteristic flow structures was found to increase at higher Womersley numbers. At expiration the axial velocity distribution contains numerous secondary vortical flow structures being generated by merging streams of the higher generation bronchi. These vortical structures increase the kinetic energy near the wall and ensure an almost perfect cleaning stream at exhalation.

The results reflect the three-dimensional flow pattern inside the highly complex geometry of a real human lung. This knowledge is essential for the improvement of artificial respiration devices and for the development of aerosol drug delivery systems. In future investigations higher generations of the lung geometry and also the upper airways will be fully modeled including the nasal cavity and the laryngeal region.

ACKNOWLEDGMENT

The support of the Deutsche Forschungsgemeinschaft (DFG) is gratefully acknowledged.

REFERENCES

[1] Zhao, Y. & Lieber, B.B., Steady expiratory flow in a model symmetric bifurcation. *Journal of Biomechanical Engineering*, **116(3)**, pp. 318–323, 1994. doi:10.1115/1.2895737

[2] Comer, J.K., Kleinstreuer, C. & Kim, C.S., Flow structures and particle desposition patterns in double-bifurcation airway models. Part 1. Air flow fields. *Journal of Fluid Mechanisms*, **435**, pp. 25–54, 2001. doi:10.1017/S0022112001003809

[3] Liu, Y., So, R.M.C. & Zhang, C.H., Modelling the bifurcating flow in a human lung airway. *Journal of Biomechanics*, **35(4)**, pp. 465–473, 2003. doi:10.1016/S0021-9290(01)00225-1

[4] van Ertbruggen, C., Hirsch, C. & Paiva, M., Anatomically based three-dimensional model of airways to simulate flow and particle transport using computational fluid dynamics. *Journal of applied physiology*, **98**, pp. 970–980, 2005. doi:10.1152/japplphysiol.00795.2004

[5] Weibel, E., *Morphometry of the Human Lung*. Springer: Berlin, 1963.

[6] Zhang, Z., Kleinstreuer, C. & Kim, C.S., Gas-solid two-phase flow in a triple bifurcation lung airway model. *International Journal of Multiphase Flow*, **28(6)**, pp. 1021–1046, 2002. doi:10.1016/S0301-9322(02)00011-3

[7] Li, Z., Kleinstreuer, C. & Zhang, Z., Particle deposition in the human tracheobronchial airways due to transient inspiratory flow patterns. *Journal of Aerosol Science*, **38(6)**, pp. 625–644, 2007. doi:10.1016/j.jaerosci.2007.03.010

[8] Nowak, N., Kakade, P.P. & Annapragada, A.V., Computational fluid dynamics simulation of airfoil and aerosol deposition in human lungs. *Annals of Biomedical Engineering*, **31**, pp. 374–390, 2003. doi:10.1114/1.1560632

[9] Lin, C.L., Tawhai, M.H., McLennan, G. & Hoffman, E.A., Characteristics of the turbulent laryngeal jet and its effect on airflow in the human intra-thoracic airways. *Respiratory Physiology & Neurobiology*, **157(2–36)**, pp. 295–309, 2007.

[10] Große, S., Schröder, W., Klaas, M., Klöckner, A. & Roggenkamp, J., Time resolved analysis of steady and oscillating flow in the upper human airways. *Experiments in Fluids*, **42**, pp. 955–970, 2007. doi:10.1007/s00348-007-0318-y

[11] Große, S., Schröder, W. & Klaas, M., Time-resolved PIV measurements of vortical structures in the upper human airways. *Particle Image Velocimetry*, volume 112/2008 of *Topics in Applied Physics*, Springer: Berlin/Heidelberg, pp. 35–53, 2008.

[12] Succi, S., *The Lattice Boltzmann Equation for Fluid Dynamics and Beyond*. Oxford University Press: Oxford, 2001.

[13] Ball, C.G., Uddin, M. & Pollard, A., Mean flow structures inside the human upper airway. *Flow, Turbulence and Combustion*, **81**, pp. 155–188, 2008. doi:10.1007/s10494-007-9113-3

[14] Freitas, R.K. & Schröder, W., Numerical investigation of the three-dimensional flow in a human lung model. *Journal of Biomechanics*, **41**, pp. 2446–2457, 2008. doi:10.1016/j.jbiomech.2008.05.016

[15] Hartmann, D., Meinke, M. & Schröder, W., An adaptive multilevel multigrid formulation for Cartesian hierarchical grid methods. *Computation Fluids*, **37**, pp. 1103–1125, 2008. doi:10.1016/j.compfluid.2007.06.007

[16] Truckenbrodt, E., *Fluidmechanik 1*. Springer-Verlag: Berlin, 1996.

[17] Dean, W.R., Note on the motion of fluid in a curved pipe. *Philosophical Magazine*, **20**, pp. 208–23, 1927.

[18] Dean, W.R., The streamline motion of fluid in a curved pipe. *Philosophical Magazine*, **30**, pp. 673–93, 1928.

[19] Berger, S.A. & Talbot, L., Flow in curved pipes. *Annual Review of Fluid Mechanisms*, **15**, pp. 461–512, 1983. doi:10.1146/annurev.fl.15.010183.002333

[20] Rütten, F., Schröder, W. & Meinke, M., Large-eddy simulation of low frequency oscillations of the Dean vortices in turbulent pipe bend flows. *Physics of Fluids*, **17(035107)**, pp. 1–11, 2005.

[21] Womersley, J.R., *An elastic tube theory of pulse transmission an oscillatory flow in mammalian arteries*. Technical report, Wright Air Development Center, 1957.

[22] Frisch, U., Hasslacher, B. & Pomeau, Y., Lattice-gas automata for the Navier Stokes equation. *Physical Review Letters*, **56(14)**, pp. 1505–1508, 1986. doi:10.1103/PhysRevLett.56.1505

[23] Benzi, R., Succi, S. & Vergassola, M., The Lattice Boltzmann equation: theory and applications. *Physics Reports*, **222(No. 3)**, pp. 145–197, 1992. doi:10.1016/0370-1573(92)90090-M

[24] Chen, S. & Doolen, G.D., Lattice Boltzmann method for fluid flows. *Annual Review of Fluid Mechanisms*, **30**, pp. 329–364, 1998. doi:10.1146/annurev.fluid.30.1.329

[25] Bhatnagar, P.L., Gross, E.P. & Krook, M., A model for collision processes in gases. I. Small amplitude processes in charged and neutral one-component systems. *Physical Review*, **94(3)**, pp. 511–525, 1954. doi:10.1103/PhysRev.94.511

[26] Hänel, D., *Molekulare Gasdynamik*, Springer: Berlin, 2004.

[27] Qian, Y.H., D'Humieres, D. & Lallemand, P., Lattice BGK models for Navier–Stokes equations. *Europhysics Letters*, **17(6)**, pp. 479–484, 1992. doi:10.1209/0295-5075/17/6/001

[28] Zou, Q., Hou, S., Chen, S. & Doolen, G.D., An improved incompressible lattice Boltzmann model for time-independent flows. *Journal of Statistical Physics*, **81(1–2)**, pp. 35–48, 1995. doi:10.1007/BF02179966

[29] Bouzidi, M., Firdaouss, M. & Lallemand, P., Momentum transfer of a Boltzmann–Lattice fluid with boundaries. *Physics of Fluids*, **13(11)**, pp. 3452–3459, 2001. doi:10.1063/1.1399290